

Supplementary Information

Capillary front broadening for water-evaporation-induced electricity of integrated one kilovolt

Wei Deng^{1,§}, Gu Feng^{2,§}, Luxian Li^{1,3}, Xiao Wang^{1,3}, Huan Lu^{1,3}, Xuemei Li^{1,2}, Jidong Li¹, Wanlin Guo^{1,4,*},
Jun Yin^{1,3,*}

¹State Key Laboratory of Mechanics and Control of Mechanical Structures, Key Laboratory for Intelligent Nano Materials and Devices of the Ministry of Education, Institute for Frontier Science, Nanjing University of Aeronautics and Astronautics, Nanjing, 210016, China.

²College of Material Science and Engineering, Nanjing University of Aeronautics and Astronautics, Nanjing, 210016, China.

³College of Aerospace Engineering, Nanjing University of Aeronautics and Astronautics, Nanjing, 210016, China.

§These authors contributed equally

*e-mail: wlguo@nuaa.edu.cn; yinjun@nuaa.edu.cn

This PDF file includes:

Fig.S1 to Fig.S28

Table S1

Supplementary Note1

Table S1 Comparison of voltage output of the devices in this work with devices reported in the literature (unit devices were connected in series for integration).

	Unit device	Integrated device			Unit device	Integrated device	
	V_{oc} (V)	V_{oc} (V)	Device number		V_{oc} (V)	V_{oc} (V)	Device number
[1]	0.28	3.44	12	[2]	0.78	2.9	5
[3]	0.3	1.2	4	[4]	0.82	8.28	10
[5]	0.39	NA	NA	[6]	0.83	3.3	4
[7]	0.4	1.75	6	[8]	0.83	2.5	3
[9]	0.4	NA	NA	[10]	1	4.2	5
[11]	0.45	5	12	[12]	1.2	4.8	4
[13]	0.53	2.38	5	[14]	1.2	3.32	3
[15]	0.6	2.4	4	[16]	1.5	3	2
[17]	0.6	NA	NA	[18]	1.5	3.7	3
[19]	0.63	2.34	6	[20]	1.63	3.39	3
[21]	0.65	1.45	4	[22]	2.5	14.8	6
[23]	0.7	2.2	3	[24]	3	5	2
[25]	0.66	3.7	6	This work	5	1200	270

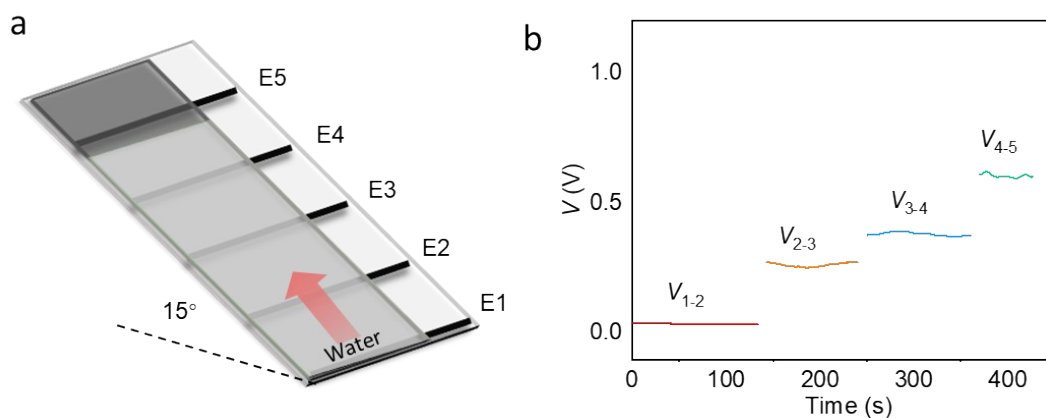


Fig. S1. Voltage output of a 5-electrode device. a, Schematic illustration of the water-evaporation-induced electricity generation device; the porous film was fabricated using carbon black nanoparticles and the electrodes by carbon nanotubes. b, Voltage output in each section. The fact that voltage output increases in the sections from wet to dry regions suggest the capillary front could be the key region to produce electricity with high efficiency.

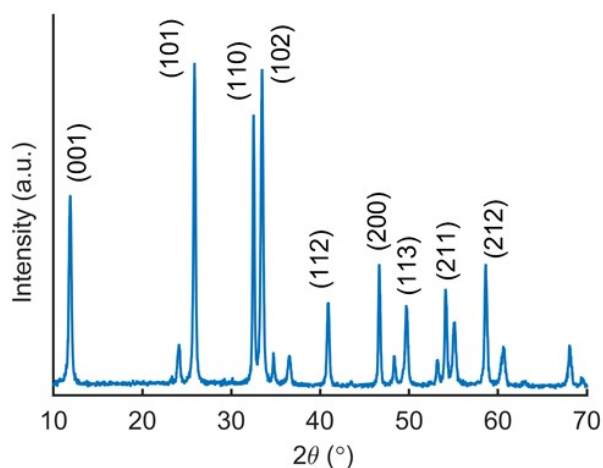


Fig. S2. XRD patterns of the as-synthesized BiOCl powder. The well-indexed sharp peaks indicate high crystallinity of the prepared BiOCl nanoplates.

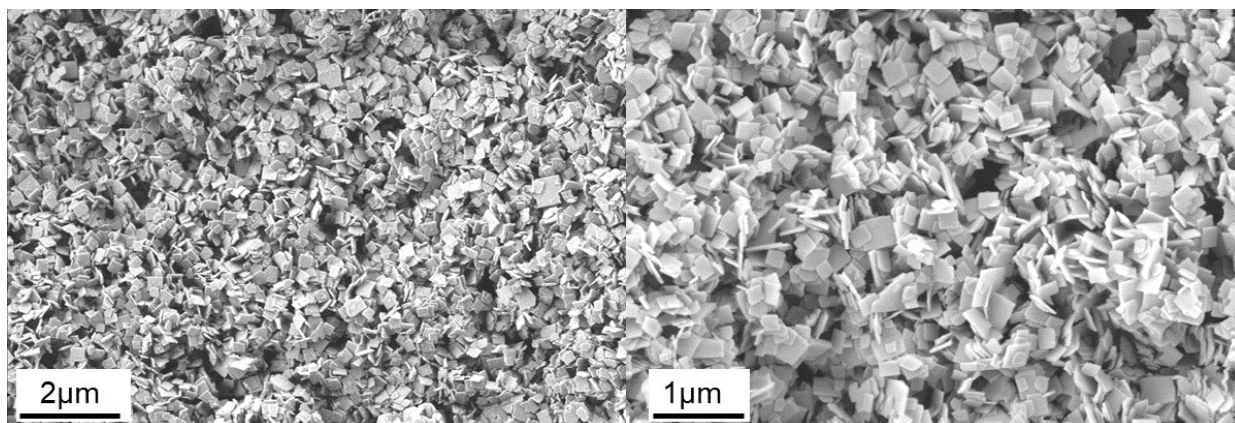


Fig. S3. SEM images of the BiOCl layer. The BiOCl nanoplates are irregularly stacked on the substrate, forming a porous layer.

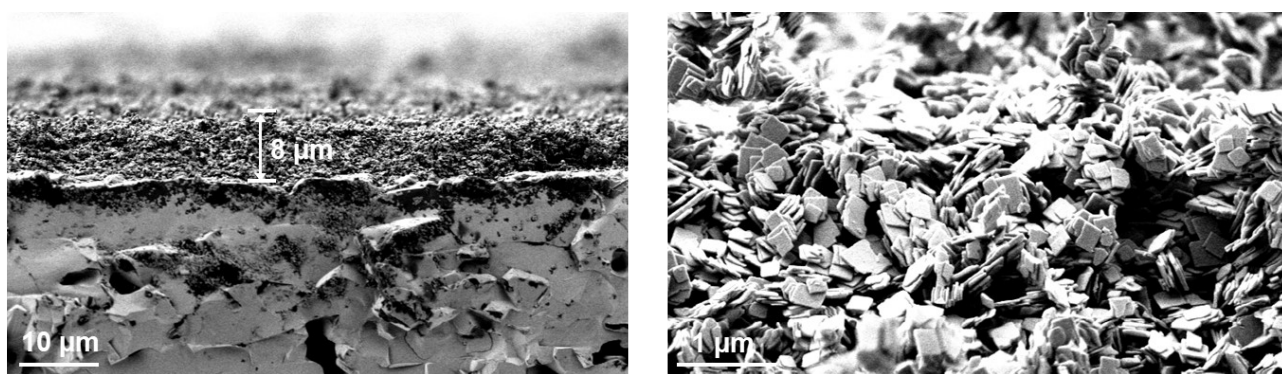


Fig. S4. Cross-sectional SEM images of the BiOCl layer. It can be seen that some BiOCl nanoplates stack almost in parallel to produce micropores and mesopores and these stacked nanoplates-clusters further form a network to generate large pores.

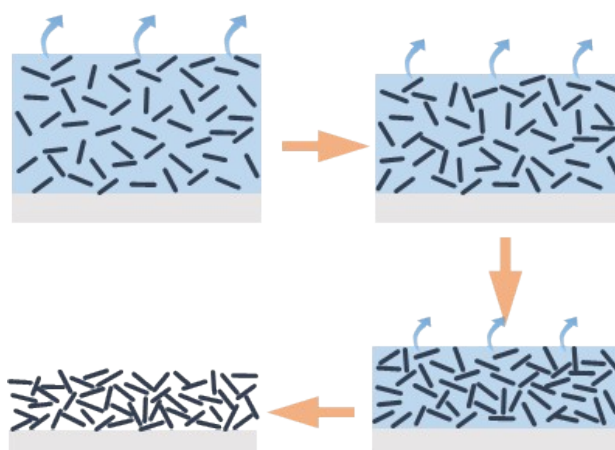


Fig. S5. Schematic illustration of evaporation-induced self-assembly of BiOCl nanoplates to produce the porous BiOCl layer.

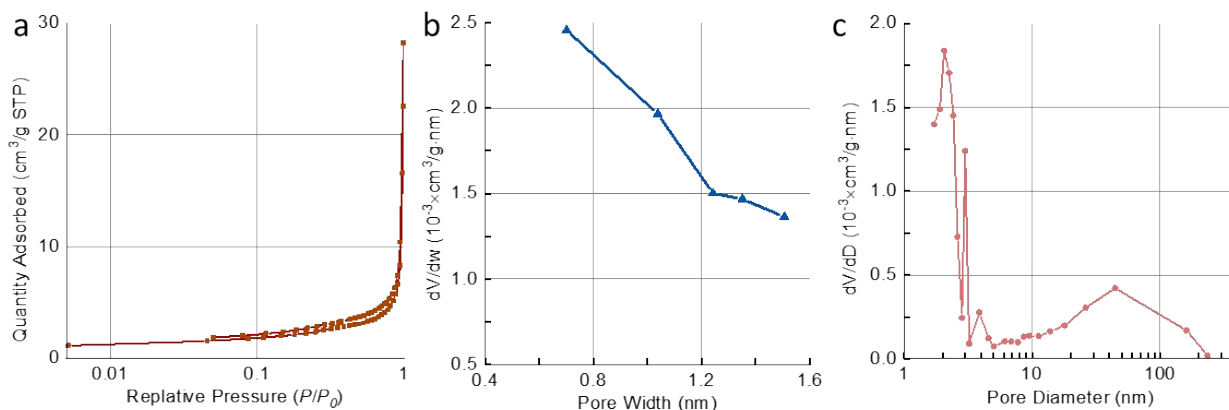


Fig. S6. Porous properties of the BiOCl layer. a, Nitrogen adsorption–desorption isotherm at 77.3 K. b and c, size distribution of the (b) micropores (H-K method) and (c) mesopores (BJH method). The data were obtained on a Micromeritics ASAP 2420 physisorption analyzer

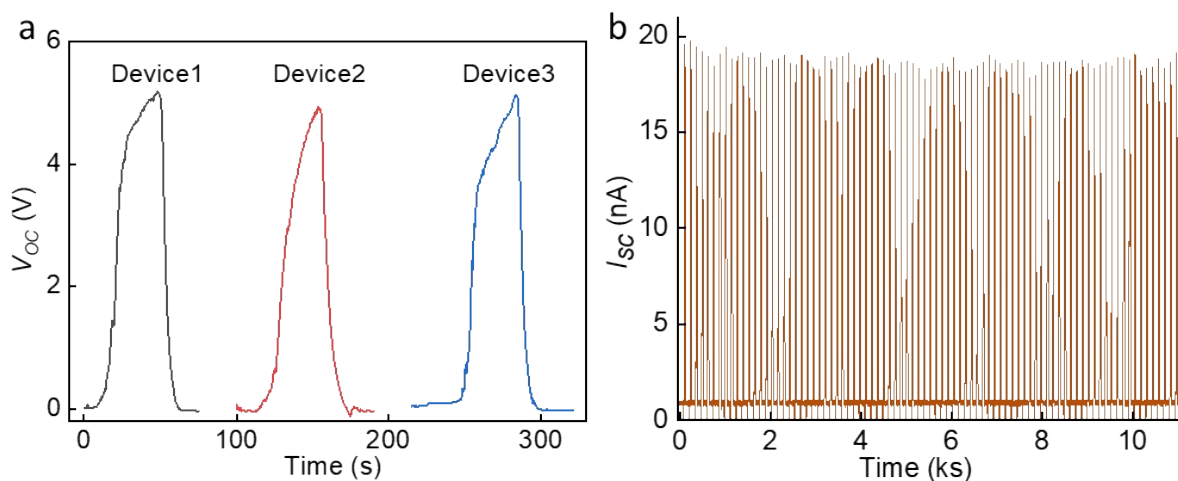


Fig. S7. a, Voltage output of three devices from different batches (8 mm X 10 mm, two-electrode), showing great consistency among the devices. b, Cyclic short-circuit current. The output current underwent negligible decrease during testing over 10 ks.

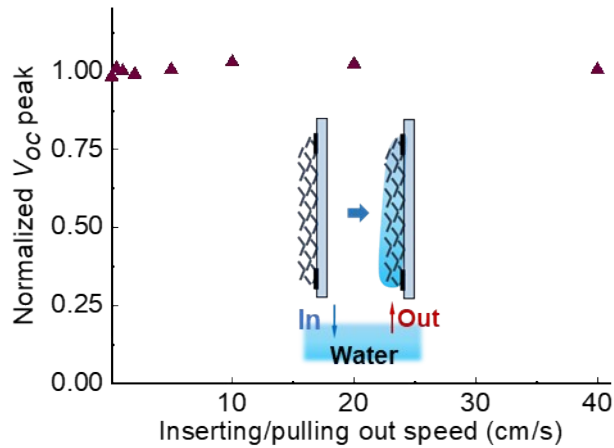


Fig. S8. Normalized voltage output under different inserting and pulling out speeds. The results indicate that the moving speed of water boundary on the BiOCl layer during inserting or pulling out does not affect the voltage output. This distinguishes the mechanism from drawing or waving potential. The results also imply low-velocity water waves can be efficiently used to form a water film on the device and generate electricity in the ensuing evaporation step, opening a new way to harvest low-velocity water waves, which are challenging to harvest by traditional resonant vibration approaches [26-28].

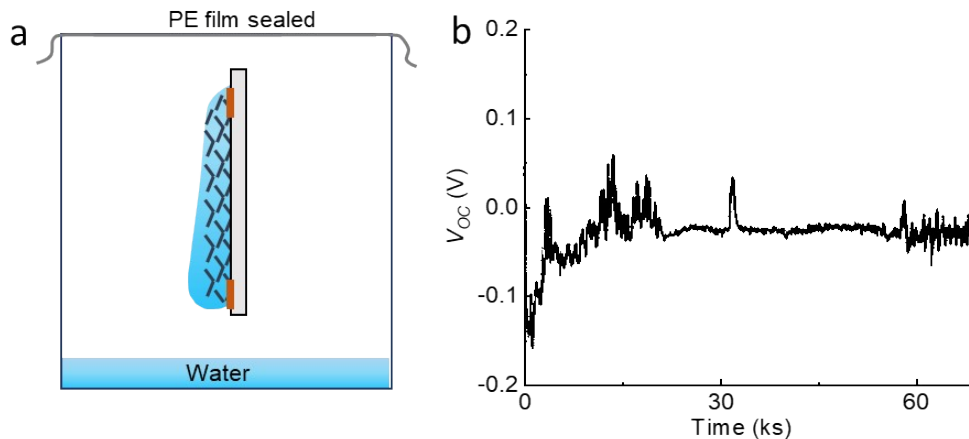


Fig. S9. Voltage output in a sealed container. a, Schematic illustration of testing setup. b, Voltage output of the device. A water film was formed before putting the device into the beaker. The measured output was about -25 mV, much lower than that at open condition, due to impeded water evaporation on the device. This highlights the origin of electricity generation is water evaporation and indicates that water flowing down due to gravity does not significantly generate electricity.

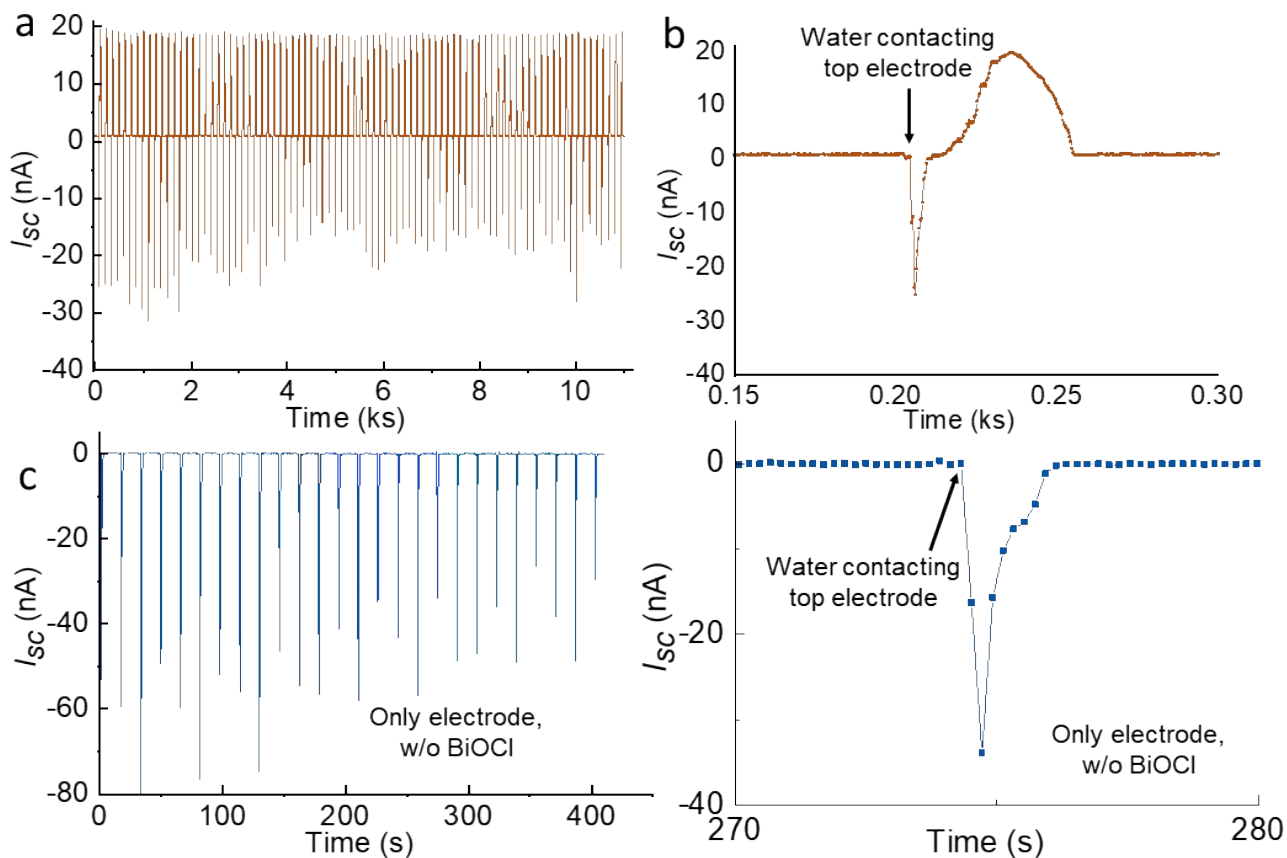


Fig. S10. Current pulses occur when water contacts the top electrode and negligible output was observed before water contacting the top electrode. a and b, Cyclic current output showing negative current pulses. c and d, Current pulses occurred even on the device without a BiOCl film. Therefore, it is not pertinent to the ensuing evaporation process and it is possibly induced by charge transfer at the water-substrate interface, which is commonly observed in water-droplet-based generators [29, 30].

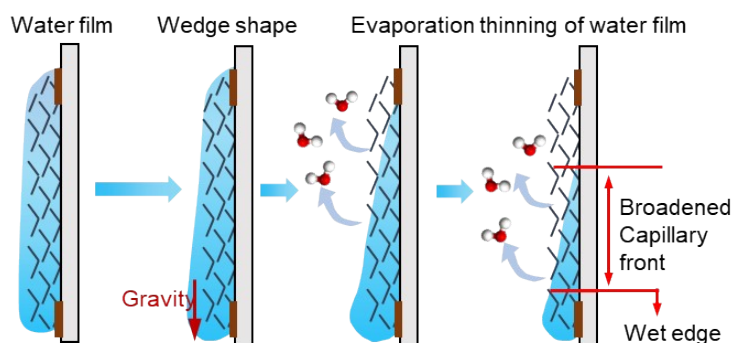


Fig. S11. Schematic illustration of the water-film operation mode and the formation of a broadened capillary front. After resting on the BiOCl layer, the water film under gravity tapers to a thin edge at the top and thickens at the bottom of the BiOCl layer, turning into a wedge shape. Meanwhile, natural evaporation keeps thinning the water film and a semi-wet region forms, transitioning from the bottom wet region to the top dry region.

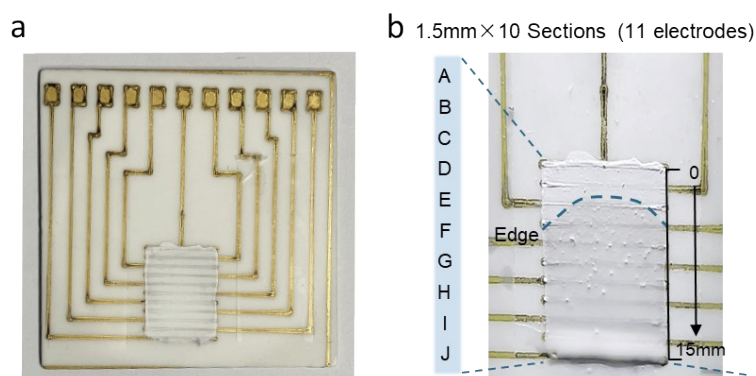


Fig. S12. The multiple-electrode device. a, Photograph of the device. b, The marked sections of the BiOCl layer. The device consists of 11 electrodes, marked as A to J from top to bottom; the electrode spacing is 1.5 mm.

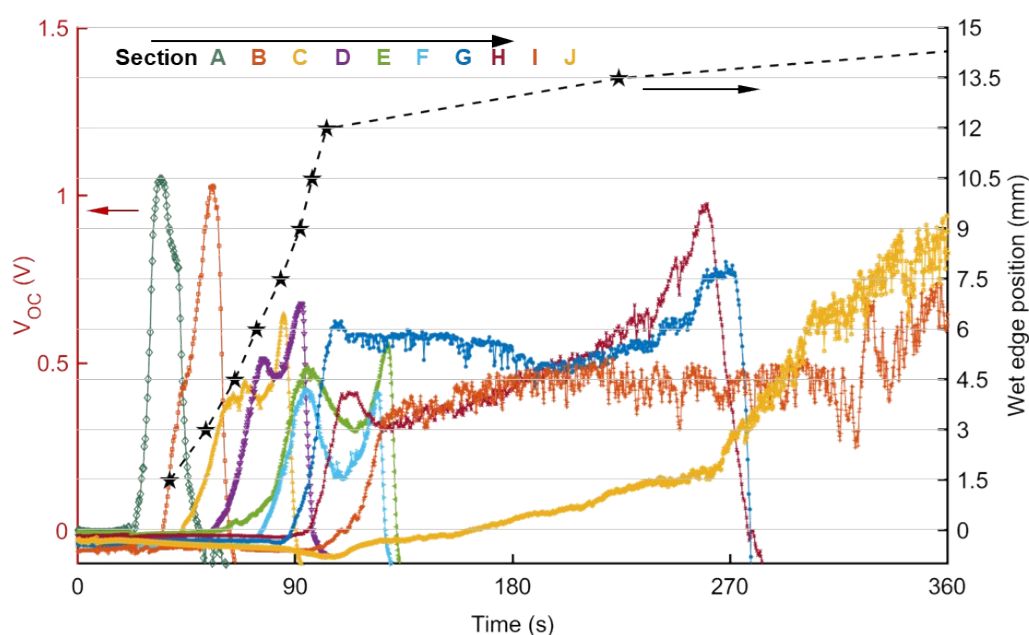


Fig. S13. Voltage output in each section and wet edge position at different time. It is clearly shown that the voltage output of a section rose up when the wet edge reached the top electrode of this section and the sections below the wet edge did not produce a notable voltage output. For example, the voltage output in the second section (the second voltage peak in the plot) started to rise up when the wet edge position reached 1.5 mm (1.5 mm corresponds to the second electrode, i.e., the top electrode of the second section). These results indicate that electricity was produced in the capillary front above the wet edge, not the full-wet region (below the wet edge). Therefore, the voltage output measured could specify the region of capillary front. The span of the capillary front was extracted from the above plots in this way. It is worth noting that the wet edge is generally curved due to faster local evaporation near the side boundaries of the BiOCl layer. We choose the edge peak as the wet edge position. Therefore, we can see voltage rising up in the sections below the wet edge position since the wet edge spans multiple sections.

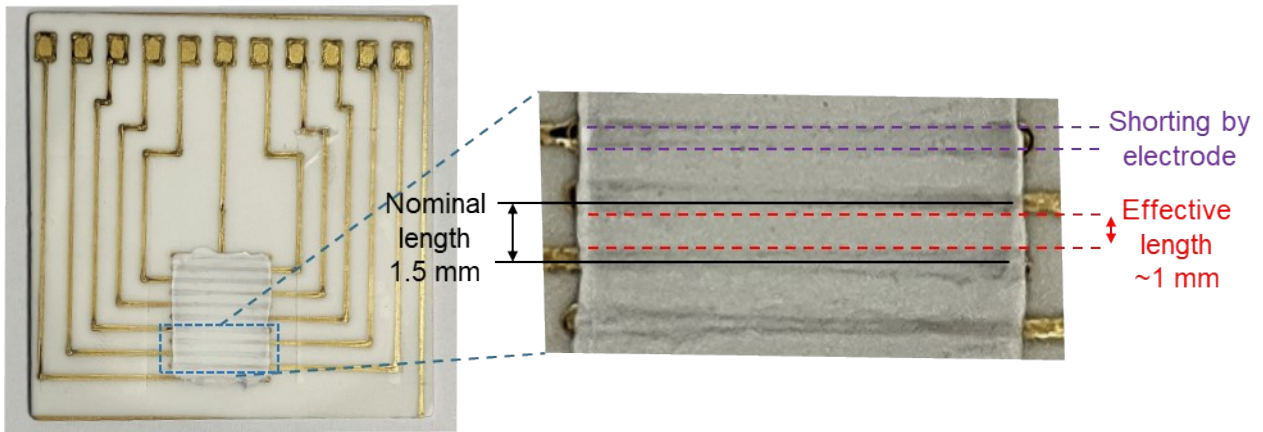


Fig. S14. Schematic illustration of the effect of Au electrodes on voltage output. The effective length of the BiOCl layer is smaller than the nominal length because of the Au electrodes. The nominal length (the distance between the center of two adjacent electrodes) of each section is 1.5 mm, however, the effective length (the distance between the edges of two adjacent electrodes) is smaller, about 10 mm. This is because the part of BiOCl layer painted right on the Au electrode produce no voltage output due to electric shorting by the electrode. The reduced length therefore leads to a narrow effective semi-wet region and lower voltage output. Therefore, the voltage output in the sections in the multiple - electrode device did not sum to 5 V. This however does not affect investigating the spatial distribution of voltage output and identifying the active regions.

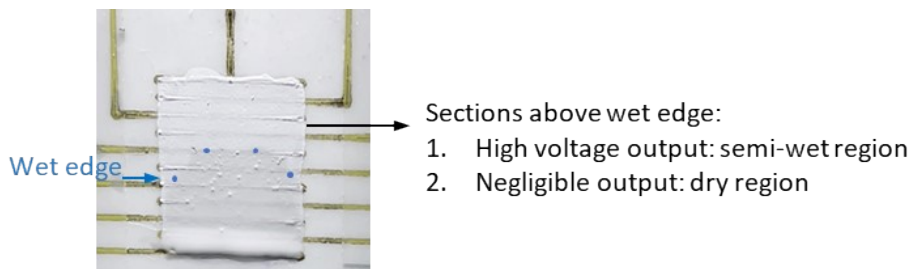


Fig. S15. Criteria for identifying the semi-wet region.

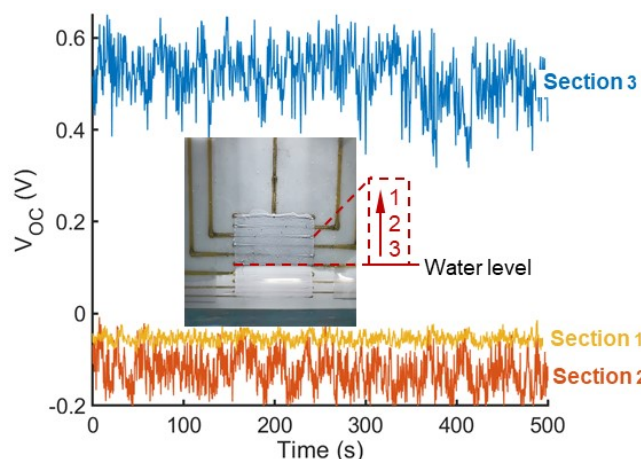


Fig. S16. Time-resolved voltage output of each section in the one-end-immersing mode. In our device, the BiOCl layer is not superhydrophilic (a contact angle of 36°), partly due to the addition of Nafion polymer as the bonding agent, therefore, the capillary height is limited ($\sim 3\text{mm}$). The wet edge is about 1.5 mm above the bulk water level and the capillary front is about 1.5 mm in length above the wet edge.

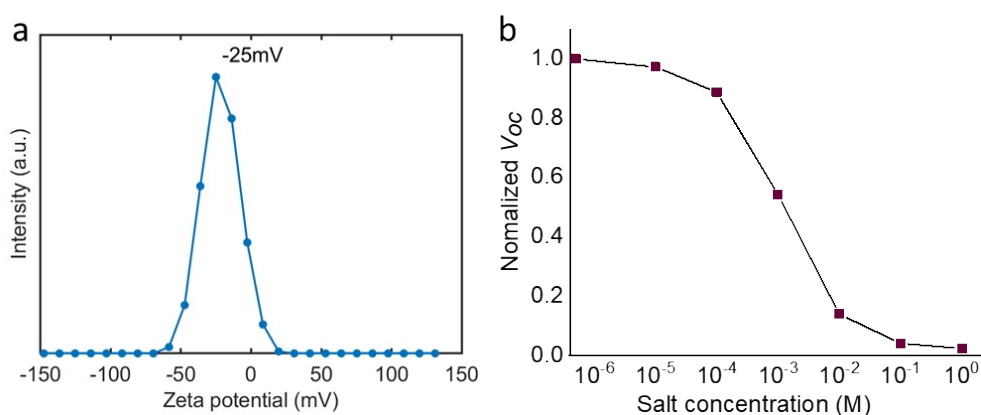


Fig. S17. Zeta potential and effects of salt concentration. a, Zeta potential of BiOCl nanoplates; b, Dependence of voltage output on salt (NaCl) concentration in water. These results are consistent with the streaming potential theory. The “normalized Voc” refers to the voltage peaks measured at different inserting/pulling out speed normalized by the voltage peak measured at a speed of $2\text{ cm}\cdot\text{s}^{-1}$ since this speed was used for the majority of the experiments.

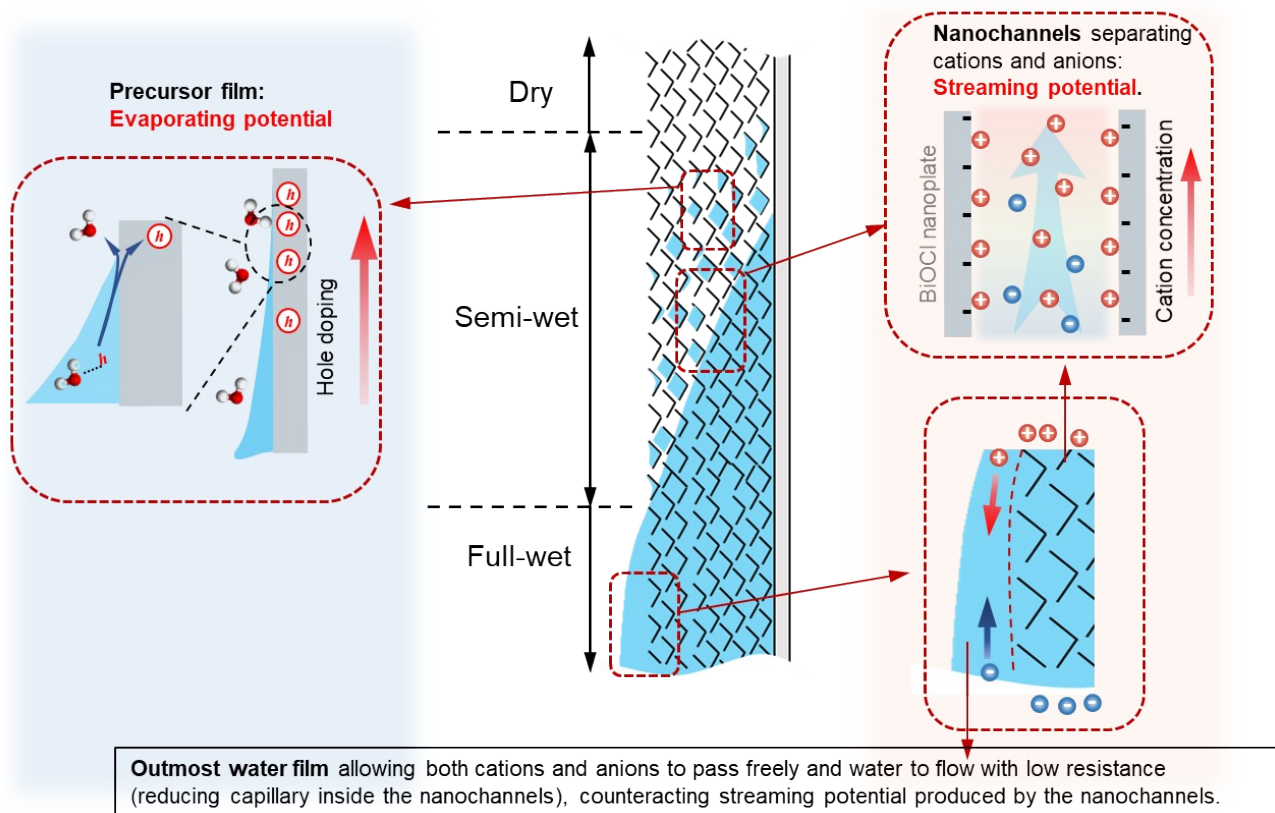


Fig. S18. Voltage generation mechanisms in the semi-wet and full-wet regions. The schematic illustration explains why the semi-wet region is more effective than the full-wet region invoking the so-far reported two mechanisms, i.e., streaming potential and evaporating potential. First, both the semi-wet and full-wet regions are rich in nanochannels and can spatially separate cations and anions, thereby producing streaming potential. However, the full-wet regions have an additional outmost water film on the BiOCl layer and this water film allows both cations and anions to pass freely. As a result, cations and anions separated by the nanochannels can diffuse backward. In addition, water flowing in the outmost water film is subject to a lower resistance than in the tortuous nanochannels inside the BiOCl layer, which diminishes water capillary inside the BiOCl layer. These two effects counteract the streaming potential produced by the nanochannels and diminish the output voltage in the full-wet regions. Second, according to the theory of evaporating potential, water evaporation in the precursor films spreading in the semi-wet region generates hole doping gradient and produces voltage output. The full-wet region, without precursor films spreading on the nanopore walls, cannot produce evaporating potential. Therefore, the semi-wet-region is more effective for voltage generation than the full-wet region.

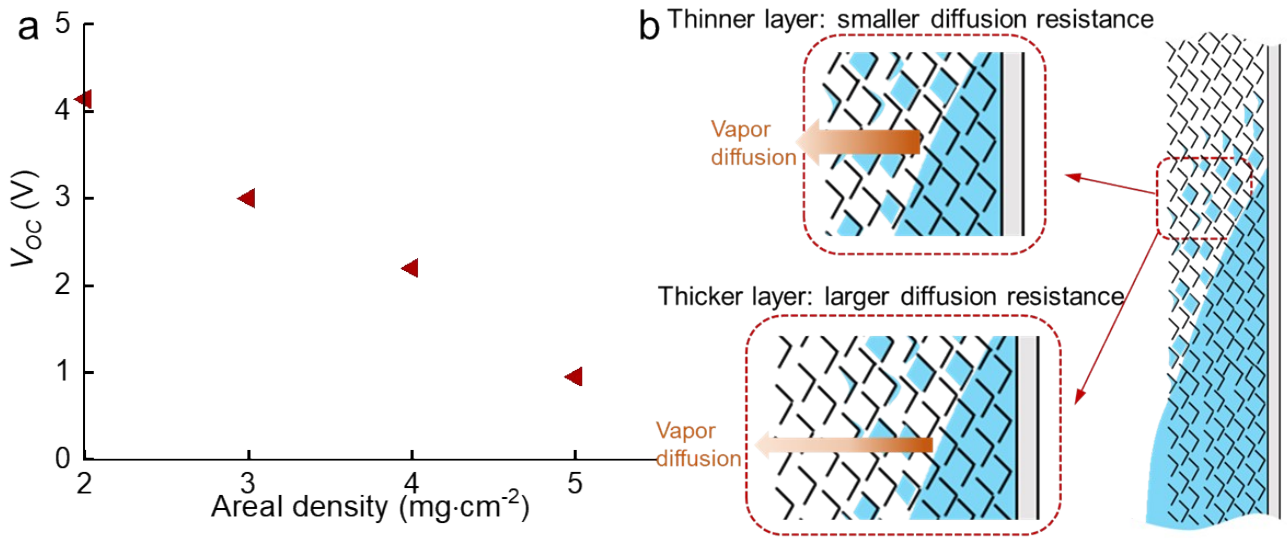


Fig. S19. Voltage output with different areal densities of the BiOCl layer and schematic illustration of water vapor diffusion resistance in the semi-wet regions with different BiOCl layer thickness. The devices were tested at RH=40%. We varied the areal density by controlling the amount of the BiOCl slurry painted on the substrate. The voltage output decreases with the increasing areal density of the BiOCl layer. This likely caused by that a thicker BiOCl layer would increase the diffusion resistance of water vapor in the nanopores and impede water evaporation in the semi-wet region,

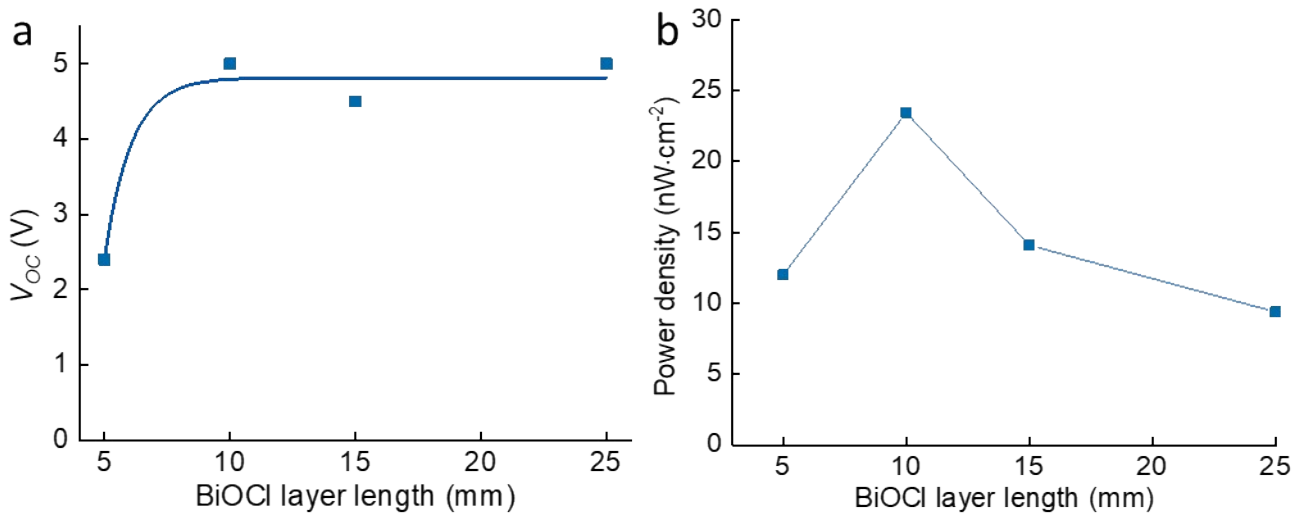


Fig. S20. Dependence of voltage output and power density on length of the BiOCl layer. The curve denotes exponential fitting. The voltage output increases from 2.4 V to 5 V when the length increases from 5 mm to 10 mm and further increasing the length to 15 mm and 25 mm does not improve the output. This is because the identified capillary front is about 6 mm. Accordingly, the 10-, 15-, and 25-mm BiOCl layers yield capillary front about 6 mm and produce similar voltage outputs, while a 5-mm-long BiOCl layer yields a narrower capillary front and a lower voltage output. The increasing of the width generally increases the current output and almost does not affect the power density. Therefore, in principle, the power density would drop to almost zero as the BiOCl layer reaches infinitely long.

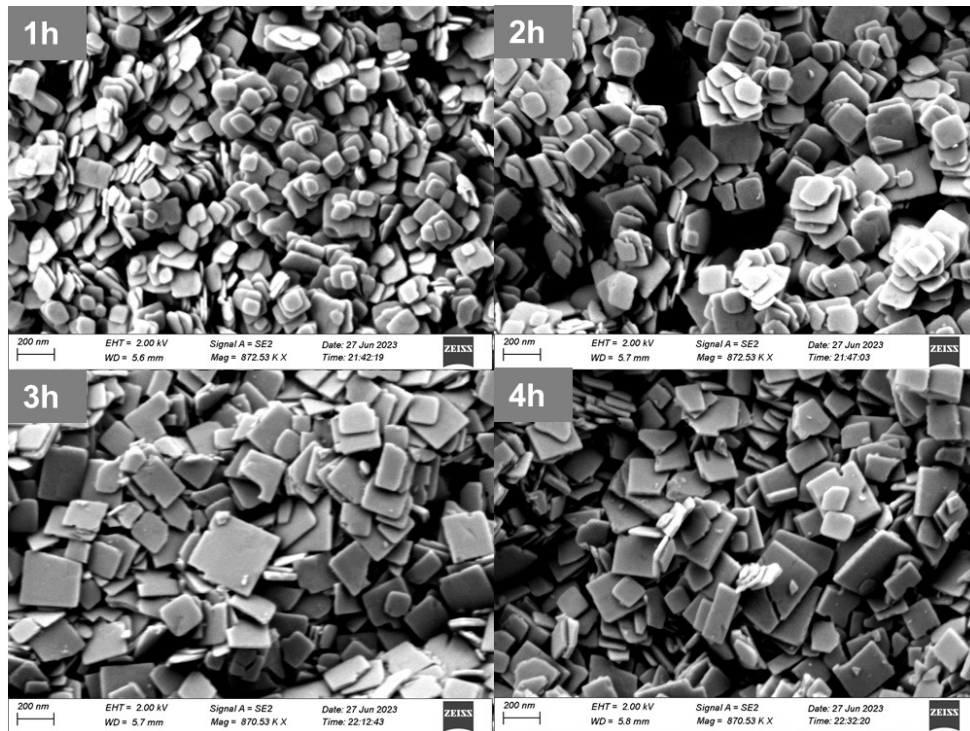


Fig. S21. SEM images of the BiOCl powder synthesized from hydrothermal treatment for different time durations (1, 2, 3, and 4 h). The planar dimension increases with the hydrothermal treatment time.

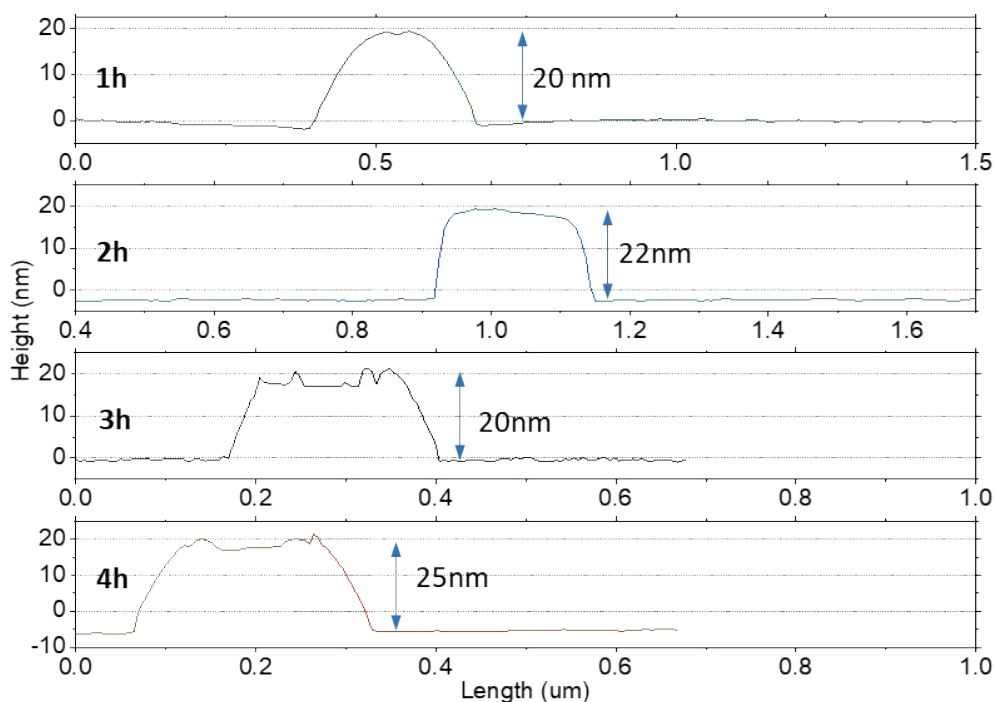


Fig. S22. Thickness profiles of the BiOCl nanoplates synthesized from hydrothermal treatment for different durations. The nanoplates have similar thickness in the range of 20 to 25 nm. The data were obtained from atomic force microscopy (SmartSPM-1000, tapping mode). The BiOCl nanoplates were synthesized by a hydrothermal approach and we varied the hydrothermal treatment time (1, 2, 3, 4 h) to control the size of the nanoplates. Because the layered structure of BiOCl tends to grow along the planar direction during hydrothermal treatment under the direction of mannitol molecules[31], a longer time produces larger planar dimensions (Fig. S21) but negligibly change the nanoplate thickness.

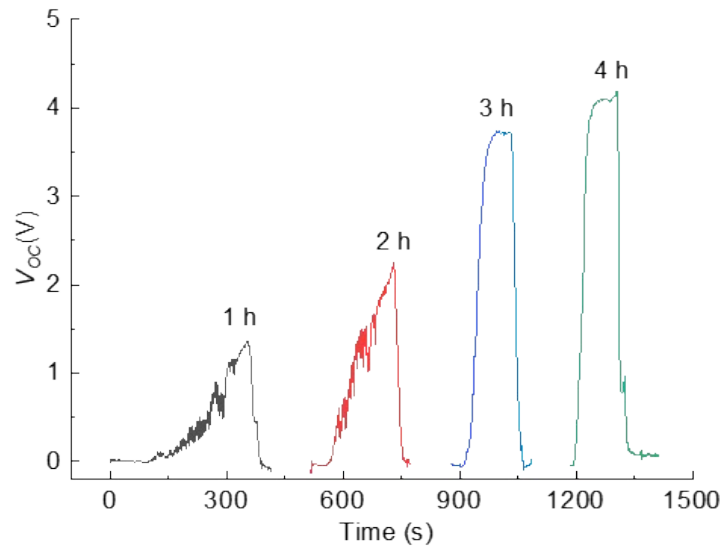


Fig. S23. Voltage output profiles of the devices made of BiOCl powder synthesized from hydrothermal treatment for different time durations. The devices were tested at RH=40%. We then tested the devices and the voltage output profiles are displayed in Fig. R5. The exhibited trend is similar to that of the planar dimensions of the BiOCl nanoplates, that is, the voltage amplitude increases significantly from the 1 h-device to 3 h-device and the 4 h-device has a slightly higher output than the 3 h-device. This can be plausibly explained as follows. The nanoplates that stack almost in parallel provide abundant micro- and mesopores and the stacked nanoplates-clusters further form a porous network to produced larger pores. The larger nanoplates provide more micro- and mesopores among the almost parallelly stacked nanoplates, while the smaller nanoplates produce more larger pores among the nanoplates-clusters. Therefore, the BiOCl nanoplates with larger planar dimensions generate higher voltage output.

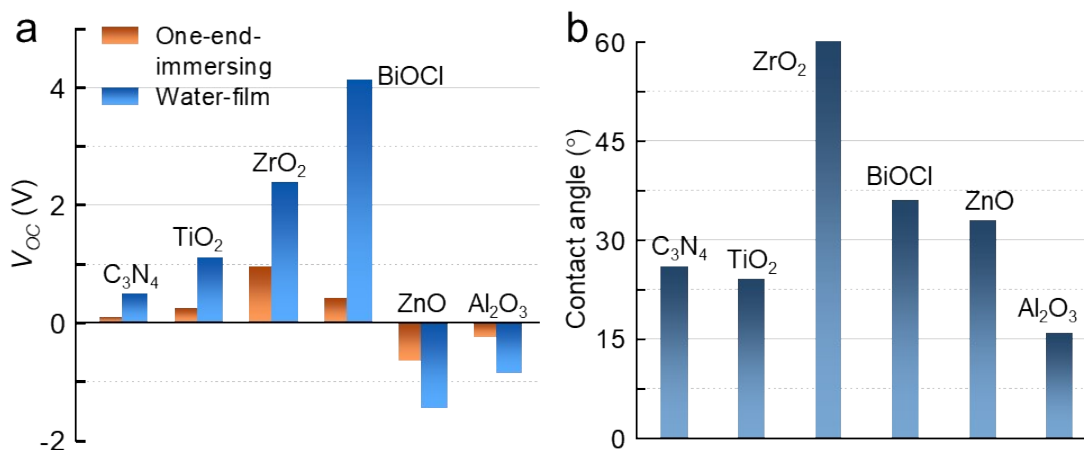


Fig. S24. a, Voltage output of different materials under water-film mode and one-end-immersing mode. All the materials showed enhanced performance under the water-film mode comparing with the conventional one-end-immersing mode. This implies that the water-film mode strategy could be generalized to devices made out of various nanomaterials. The devices were tested at RH=40%. b, contact angles of the films made of different materials.

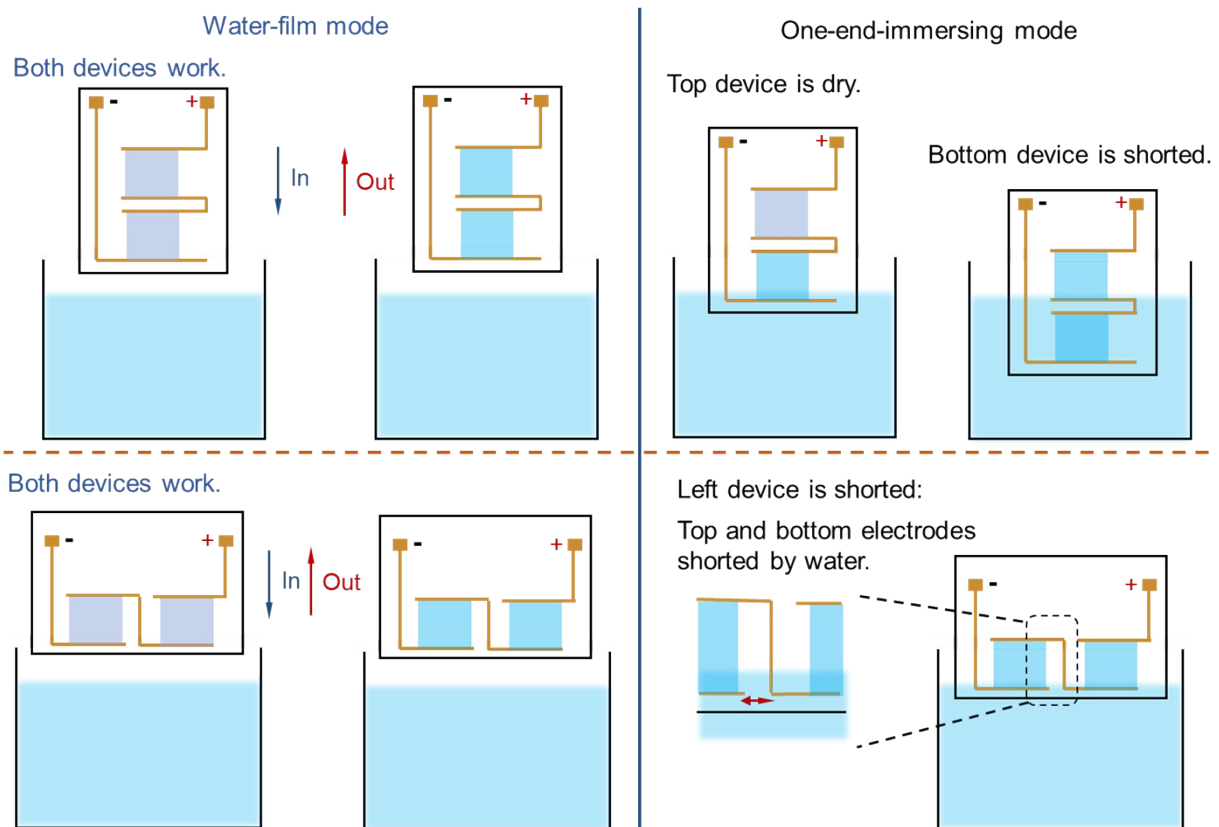


Fig. S25. Schematic illustration of two serial-connected devices working under the water-film mode and one-end-immersing mode. We used the integration of two devices as an example. When two serial-connected devices are integrated with a top-down configuration, both devices can work under the water-film mode. However, only one device can work under the one-end-immersing mode, because either the top device is dry (lacks water reservoir) or the bottom one is shorted (fully immersed in water in order to wet the top device). When the two devices are integrated with a side-by-side configuration, both devices work under the water-film mode. However, only one device can work under the one-end-immersing mode, because the left device is shorted by water (both the top and bottom electrodes are in contact with water). Therefore, only one water reservoir is required for integrated devices under the water-film mode, while separate water reservoirs are necessary for the one-end-immersing mode, which impedes device integration especially for high voltage output.

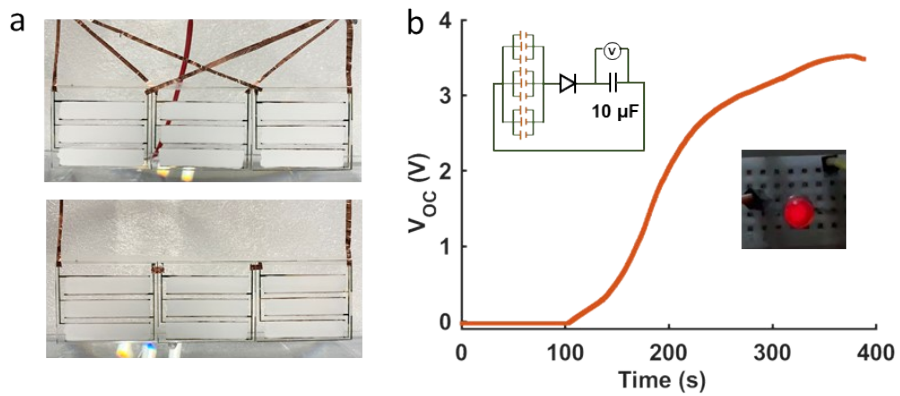


Fig. S26. Electrical output of the integrated devices. a, Photographs of the integrated devices. The top one consists of 9 unit device ($5\text{ cm} \times 1\text{ cm}$ each) connected in parallel; the bottom one consists of 3 groups of devices (3 unit device connected in parallel in each group) connected in series. b, Charging curve of a $10\ \mu\text{F}$ capacitor powered by 9 unit device ($5\text{ cm} \times 1\text{ cm}$ each) connected in parallel. The inset shows an LED lighted up by the charged capacitor.

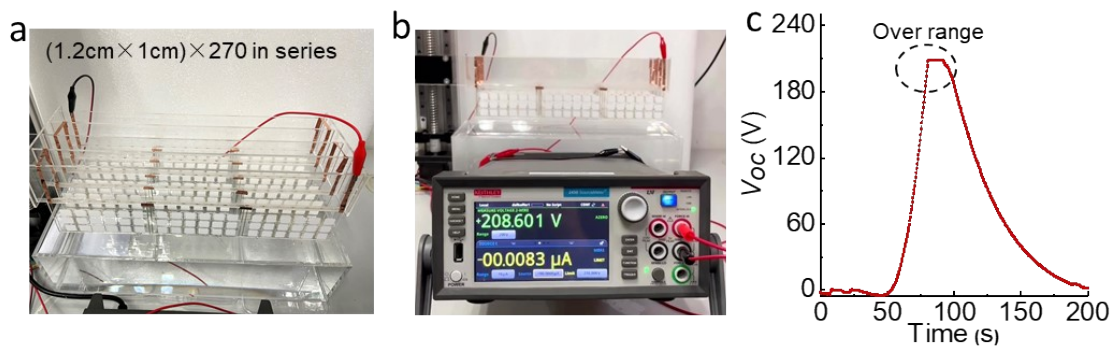


Fig. S27. High voltage output of integrated devices. a, Photograph of the integrated device. b, Voltage output directly recorded on a Keithley 2450 source meter, which has a nominal measurable range of 0 - 200 V. c, Voltage output exceeds the measurable range of the source meter.

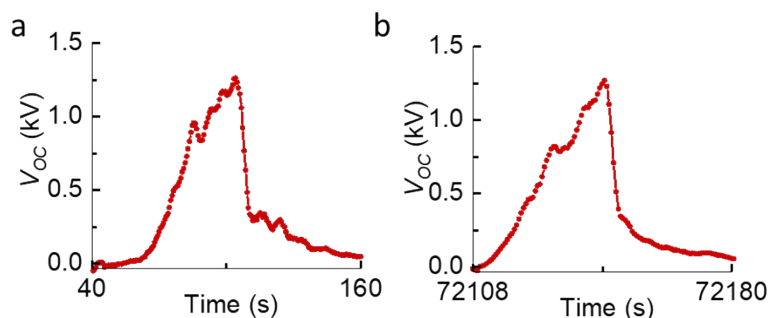


Fig. S28. High voltage output of the integrated devices connected with matched resistance. a and b show one-cycle voltage profiles at ~ 100 s and ~ 20 h during the cyclic test.

Supplementary note1

For a few isolated water molecules scattering over the BiOCl surface as shown in the top right of Fig. 4d (in the manuscript), H₂O molecules cannot form hydrogen-bond networks, and interact with both Cl atoms at the outmost layer and Bi atoms at the sub-outer layer. In that case, H in H₂O donates electrons to the Cl while O in H₂O accepts electrons from the Bi at the same time, achieving a general balance of the total electrons in H₂O molecules. When increasing the water density to (H₂O)₄ on the (BiOCl)₈ substrate, the hydrogen-bond networks in water begin to form and pull the H₂O molecules to one plane above the substrate, which weakens the interaction between H₂O and the Bi atoms on the sub-outer layer of BiOCl. In the case of (H₂O)₈ on the (BiOCl)₈ substrate, which agrees with the H₂O density in the liquid water, H₂O-H₂O hydrogen bonds are strong enough to present a two-dimensional tetragonal H₂O network, showing a pure electron doping to the BiOCl substrate via interacting with the outmost Cl. Besides, a BiOCl flake covered by the H₂O layer with a density gradient from 8:8 to 1:8 is simulated as well in the left part in Fig.4d (in the manuscript), in which the charge redistribution shows a transformation from electrons doping to holes doping to the substrate along the density decreasing direction. Notably, the holes doping to Cl at the low H₂O density end results from the large electrons doping of the rest part, which may help us understand the dynamic process of the evaporating potential.

Before the electric appliance is introduced, the potential difference of the two ends maintains as the water hydrogen-bond networks nearest to the BiOCl surface is expected untouched according to the theory of electrical double layer. When two ends of BiOCl are connected, the electrons would flow from the wet end to the dry end showing the electric current from the dry end to the wet end. Meanwhile, the hydrogen-bond networks collapse while the hole doping is introduced to H₂O molecules at the wet end. H₂O molecules with slight hole doping flow towards the dry end and recombine with electrons there because of the evaporating process. After electrons being brought out from the substrate during evaporation, other neutral H₂O molecules would occupy the pristine BiOCl surface immediately. In such a way, the whole dynamic process of the evaporating potential is complete. During this dynamic process, the abundant gas-liquid-solid interfaces provide plenty of

sites for H₂O molecules to interact with BiOCl and achieve charge transfer with BiOCl before evaporation. This key feature enabled by the capillary front would greatly promote effects, such as evaporating potential, to augment electrical output.

References

1. Tabrizzadeh, T., et al., *Water-Evaporation-Induced Electric Generator Built from Carbonized Electrospun Polyacrylonitrile Nanofiber Mats*. ACS Applied Materials & Interfaces, 2021. **13**(43): p. 50900-50910.
2. Tan, J., et al., *Self-sustained electricity generator driven by the compatible integration of ambient moisture adsorption and evaporation*. Nature Communications, 2022. **13**(1): p. 3643.
3. Zhou, X., et al., *Harvesting Electricity from Water Evaporation through Microchannels of Natural Wood*. ACS Applied Materials & Interfaces, 2020. **12**(9): p. 11232-11239.
4. Shao, B., et al., *Electron-Selective Passivation Contacts for High-Efficiency Nanostructured Silicon Hydrovoltaic Devices*. Advanced Materials Interfaces, 2021. **8**(18): p. 2101213.
5. Wang, C., et al., *Construction of hierarchical and porous cellulosic wood with high mechanical strength towards directional Evaporation-driven electrical generation*. Chemical Engineering Journal, 2022: p. 140568.
6. Shao, B., et al., *Boosting electrical output of nanostructured silicon hydrovoltaic device via cobalt oxide enabled electrode surface contact*. Nano Energy, 2023. **106**: p. 108081.
7. Qin, Y., et al., *Constant electricity generation in nanostructured silicon by evaporation-driven water flow*. Angewandte Chemie, 2020. **132**(26): p. 10706-10712.
8. Wu, M., et al., *Printed Honeycomb-Structured Reduced Graphene Oxide Film for Efficient and Continuous Evaporation-Driven Electricity Generation from Salt Solution*. ACS Applied Materials & Interfaces, 2021. **13**(23): p. 26989-26997.
9. Yoon, S.G., et al., *Natural Evaporation-Driven Ionovoltaic Electricity Generation*. ACS Applied Electronic Materials, 2019. **1**(9): p. 1746-1751.
10. Ding, T., et al., *All-printed porous carbon film for electricity generation from evaporation-driven water flow*. Advanced Functional Materials, 2017. **27**(22): p. 1700551.
11. Liu, X., et al., *Microbial biofilms for electricity generation from water evaporation and power to wearables*. Nature Communications, 2022. **13**(1): p. 4369.
12. Xue, G., et al., *Water-evaporation-induced electricity with nanostructured carbon materials*. Nature Nanotechnology, 2017. **12**(4): p. 317-321.
13. Hu, Q., et al., *Water evaporation-induced electricity with Geobacter sulfurreducens biofilms*. Science Advances, 2022. **8**(15): p. eabm8047.
14. He, H., et al., *A water-evaporation-induced self-charging hybrid power unit for application in the Internet of Things*. Science Bulletin, 2019. **64**(19): p. 1409-1417.
15. Shao, B., et al., *Bioinspired Hierarchical Nanofabric Electrode for Silicon Hydrovoltaic Device with Record Power Output*. ACS Nano, 2021. **15**(4): p. 7472-7481.
16. Zhao, X., et al., *Robust and flexible wearable generator driven by water evaporation for sustainable and portable self-power supply*. Chemical Engineering Journal, 2022. **434**: p. 134671.
17. Wang, Z., et al., *Hierarchical Oriented Metal–Organic Frameworks Assemblies for Water-Evaporation Induced Electricity Generation*. Advanced Functional Materials, 2021. **31**(47): p. 2104732.
18. Shao, B., et al., *Freestanding silicon nanowires mesh for efficient electricity generation from evaporation-induced water capillary flow*. Nano Energy, 2022. **94**: p. 106917.

19. Zhang, G., et al., *Harvesting environment energy from water-evaporation over free-standing graphene oxide sponges*. Carbon, 2019. **148**: p. 1-8.
20. Ma, Q., et al., *Rational design of MOF-based hybrid nanomaterials for directly harvesting electric energy from water evaporation*. Advanced Materials, 2020. **32**(37): p. 2003720.
21. Xie, J., Y. Wang, and S. Chen, *Textile-Based Asymmetric Hierarchical Systems for Constant Hydrovoltaic Electricity Generation*. Chemical Engineering Journal, 2022. **431**: p. 133236.
22. Shao, C., et al., *Large-scale production of flexible, high-voltage hydroelectric films based on solid oxides*. ACS applied materials & interfaces, 2019. **11**(34): p. 30927-30935.
23. Sun, J., et al., *Electricity generation from a Ni-Al layered double hydroxide-based flexible generator driven by natural water evaporation*. Nano Energy, 2019. **57**: p. 269-278.
24. Li, J., et al., *Surface functional modification boosts the output of an evaporation-driven water flow nanogenerator*. Nano Energy, 2019. **58**: p. 797-802.
25. Li, L., et al., *Sustainable and flexible hydrovoltaic power generator for wearable sensing electronics*. Nano Energy, 2020. **72**: p. 104663.
26. Deng, W. and Y. Wang, *Non-contact magnetically coupled rectilinear-rotary oscillations to exploit low-frequency broadband energy harvesting with frequency up-conversion*. Applied Physics Letters, 2016. **109**(13): p. 133903.
27. Deng, W. and Y. Wang, *Systematic parameter study of a nonlinear electromagnetic energy harvester with matched magnetic orientation: Numerical simulation and experimental investigation*. Mechanical Systems and Signal Processing, 2017. **85**: p. 591-600.
28. Deng, W., T. Fan, and Y. Li, *Water wave vibration-promoted solar evaporation with super high productivity*. Nano Energy, 2022. **92**: p. 106745.
29. Li, X., et al., *Performance and power management of droplets-based electricity generators*. Nano Energy, 2022. **92**: p. 106705.
30. Xu, W., et al., *A droplet-based electricity generator with high instantaneous power density*. Nature, 2020. **578**(7795): p. 392-396.
31. Xiong, J., et al., *Well-crystallized square-like 2D BiOCl nanoplates: mannitol-assisted hydrothermal synthesis and improved visible-light-driven photocatalytic performance*. RSC advances, 2011. **1**(8): p. 1542-1553.